A Dual-Frequency Dual-Load Multirelay Magnetic Coupling Wireless Power Transfer System Using Shared Power Channel

Xinyu Hou, Zhihui Wang, *Member, IEEE*, Yugang Su, *Member, IEEE*, Zhe Liu, and Zhipeng Deng

***Abstract*—Aiming at the power supply solution of online monitoring equipment for high-voltage transmission lines, a dual-frequency dual-load multirelay magnetic coupling wireless power transfer (MC-WPT) system using a shared power channel has been proposed. The proposed MC-WPT system provides the selective power distribution for different loads and has the constant current output characteristic. First, a dual-frequency inverter is introduced to provide the ac voltage of two frequencies. The compensation network that includes the band-stop filter can reduce the cross interference of the nontarget frequency from another power channel. Second, the system is modeled and analyzed based on the quadratic eigenvalue problem. Considering the cross-coupling mutual inductance, operating frequencies that make the system have constant current output characteristics are obtained. Finally, three evaluation indices are proposed: average current gain, load-independent index, and average sensitivity index of operating frequencies. Optimized operating frequency is selected according to these evaluation indices. The experimental results verify constant current output characteristics and the selective power distribution of two power channels.**

***Index Terms*—Evaluation index, multirelay, online monitoring equipment, quadratic eigenvalue problem, selective power distribution, wireless power transfer (WPT).**

I. Introduction

The online monitoring equipment installed on the high-voltage transmission lines (HVTLs) is becoming more and more important in the smart grid [1]–[3]. The online monitoring equipment provides real-time monitoring and analysis of parameters, such as temperature, humidity, wind speed, tower tilt, and icing, to provide early warning of abnormal HVTL conditions. A reliable and stable dc power supply is urgently required for the online monitoring equipment to operate 24 h a day.

Manuscript received 18 March 2022; revised 30 May 2022; accepted 3 July 2022. Date of publication 12 July 2022; date of current version 6 September 2022. This work was supported by the National Natural Science Foundation of China under Grant 51977015. Recommended for publication by Associate Editor C. K. Lee. *(Corresponding author: Zhihui Wang.)*

Xinyu Hou, Zhe Liu, and Zhipeng Deng are with the College of Automation, University of Chongqing, Chongqing 400044, China. (e-mail: 1226879853@qq.com; 809632730@qq.com; 1126421395@qq.com).

Zhihui Wang and Yugang Su are with the China National Center for International Research on Wireless Power Transfer Technology, Chongqing 400044, China, and also with the College of Automation, University of Chongqing, Chongqing 400044, China. (e-mail: wzhcqu@hotmail.com; su7558@qq.com).

Color versions of one or more figures in this article are available at https://doi.org/10.1109/TPEL.2022.3190143.

Digital Object Identifier 10.1109/TPEL.2022.3190143

Nowadays, magnetic coupling wireless power transfer (MC-WPT) technology has been a research hotspot [4]–[8]. With the advantages of safety, reliability, and flexibility, this technology has been widely used in biomedical implant equipment [9], [10], electric vehicles [11], [12], and other fields. The combination of the wireless power transfer (WPT) and the energy harvester provides a new power supply solution for the online monitoring equipment [13], [14]. The MC-WPT system transfers energy from the high voltage to the low voltage. This method overcomes the limitations of unstable weather and geographical location, which is currently one of the most promising and potential solutions. Various types of online monitoring equipment are installed on the HVTL; hence, it is necessary to supply power for multiple loads.

For the nonrelay MC-WPT system, to improve the system's suitability for online monitoring equipment, optimization methods include constraining power flow path [15] and natural frequency optimization [16]. However, the difficulty in increasing transmission distance limits its application in online monitoring equipment [17]–[19]. The coil size in the online monitoring equipment on HVTL is limited, so the reduction of the coupling coefficient in a longer transmission distance can cause the reduction of output power and efficiency. The advantage of the multirelay MC-WPT system is more prominent in terms of transmission distance. Based on the domino-resonator WPT system, a structure consisting of coil resonators embedded inside totally sealed insulation discs, has been proposed [13]. Printed circuit board resonators are covered by the composite insulation material forming the high-voltage insulator with WPT capability in [20].

It should be noted that the power consumption of online monitoring equipment varies, so the load-independent output characteristic is important for the online monitoring equipment. The load-independent output characteristic can be achieved by the compensating network design. A compensation network with multiple resonating frequencies for multiple-pickup WPT systems has been proposed in [21]. A magnetic structure is designed to omit the coupling coefficients between the nonadjacent coils, and the constant current characteristics are realized based on series and *LCC* compensation topology [22], [23].

The power demand of the online monitoring equipment is mostly concentrated on the receiver of a WPT system. The compensation network on the relay coil can be simplified to

reduce the system complexity, which is beneficial to embed the relay coil inside the insulator. In addition, cross-coupling mutual inductances and equivalent series resistance (ESR) of coils may cause system resonant frequency shift [24], so cross-coupling mutual inductances and ESR should not be ignored.

Briefly, selective power distribution for multiple loads and load-independent output characteristics need to be urgently solved in the multirelay MC-WPT system with nonnegligible cross-coupling mutual inductances for the online monitoring equipment. Followed by the idea of the signal multiplex, this article aims to achieve selective power transmission for multiple loads at multiple frequencies in the multirelay MC-WPT system [25]–[28].

The scenario of this article originates from an engineering project of HVTL that required powering two separate loads, so only two loads are considered. Two loads require constant current output characteristics. A dual-frequency dual-load multirelay MC-WPT system based on the shared power channel has been proposed, which focuses on the following.

1) Two operating frequencies are introduced to realize selective power distribution for two loads. The compensation network with the band-stop filter can reduce cross interference from the nontarget frequency.
2) The system is modeled and analyzed based on the quadratic eigenvalue problem, and the operating frequencies of the constant current output characteristic can be obtained.
3) Three evaluation indices are proposed to compare the output characteristic at different operating frequencies. They include the average gain, the load-independent index, and the average sensitivity index of operating frequency.

The rest of this article is organized as follows. The system modeling and analysis are developed in Section II. The analysis of constant current output characteristics is addressed in Section III. Followed by Section IV, the prototype is built to validate the feasibility of theoretical analysis. Finally, Section V concludes this article.

II. System Modeling and Analysis

A. System Description

The topology of a dual-frequency dual-load multirelay MC-WPT system for HVTL online monitoring equipment is shown in Fig. 1. The whole system consists of the magnetic energy harvester, an ac–dc converter, a dual-frequency inverter, the compensation networks, the coupler, two high-frequency ac–dc converters, and two loads. The relay coils are embedded in the insulator. The magnetic energy harvester is mounted on the HVTL to harvest the alternating magnetic field energy. A dual-frequency inverter is utilized to generate two high-frequency ac sources for the Tx coil. The rectifier in each power channel converts the ac power from the Rx coil to dc power for the online monitoring equipment.

The circuit of the dual-frequency dual-load multirelay MC-WPT system based on a shared power channel is shown in Fig. 2. The magnetic energy harvester and the ac–dc converter are represented by a dc voltage source V. S_1 and S_3 denote

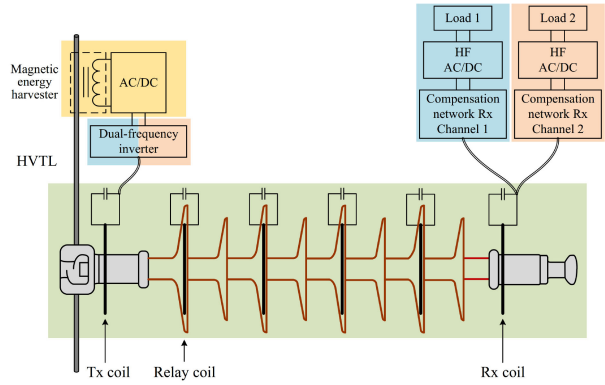

Fig. 1. Dual-frequency dual-load multirelay MC-WPT system for online monitoring equipment on HVTL.

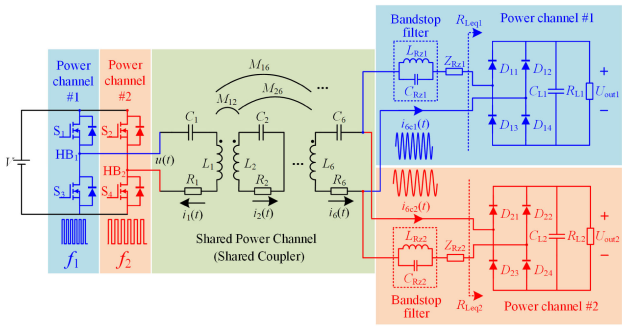

Fig. 2. Topology of a dual-frequency dual-load multirelay MC-WPT system based on shared power channel.

the half-bridge inverter HB_1. S_2 and S_4 denote the half-bridge inverter HB_2. Six coils compose the coupler. L_k and R_k represent the self-inductance and resistance of the kth coil ($k = 1, 2, \ldots, 6$), respectively. C_k represents the compensation capacitor of L_k. M_{ij} represents the mutual inductance between the ith coil and the jth coil ($M_{ij} = M_{ji}$). D_{11}, D_{12}, D_{13}, and D_{14} compose the rectifier of power channel #1, and D_{21}, D_{22}, D_{23}, and D_{24} compose the rectifier of power channel #2. C_{L1} and C_{L2} represent the filter capacitors. R_{L1} and R_{L2} represent the load resistances.

B. Working Principle

In the dual-frequency inverter, two operating frequencies are generated and controlled. ω_1 and ω_2 represent the switching frequencies of HB_1 and HB_2. They are also the operating frequencies of two power channels. Fig. 3 shows the switching sequence of the dual-frequency inverter. When S_1 and S_4 turn ON, the output of the inverter is V, when S_2 and S_3 turn ON, the output of the inverter is $-V$; otherwise, the output of the inverter is 0 V. T_1 and T_2 represent the switching periods corresponding to ω_1 and ω_2, respectively.

$u(t)$ represents the output voltage of the inverter and can be decomposed into the form of the Fourier infinite series. Because of good low-pass filtering characteristics of the proposed system, the high-order harmonics of $u(t)$ can be effectively eliminated. $u(t)$ is expressed as (1). $u_1(t)$ and $u_2(t)$ represent the equivalent

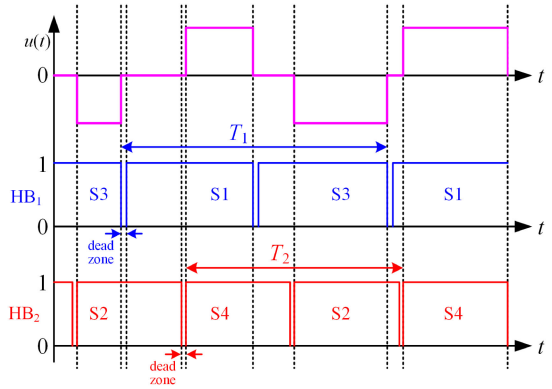

Fig. 3. Switching sequence of a dual-frequency inverter.

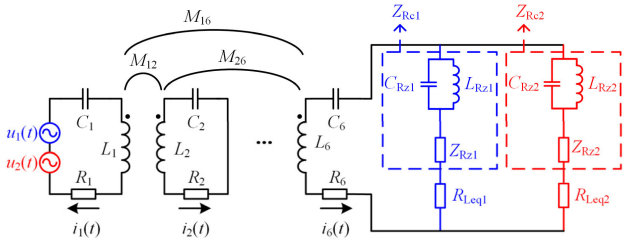

Fig. 4. Equivalent circuit of a dual-frequency dual-load multirelay MC-WPT system based on shared power channel.

voltage sources of HB_1 and HB_2, which are expressed as (2)

$$u(t) = u_1(t) - u_2(t) \tag{1}$$

$$\begin{cases} u_1(t) = \frac{2}{\pi} V \sin(\omega_1 t) \\ u_2(t) = \frac{2}{\pi} V \sin(\omega_2 t). \end{cases} \tag{2}$$

Thus, we can get the equivalent circuit of the system based on the shared power channel, as shown in Fig. 4.

R_{Leq1} and R_{Leq2} represent the equivalent load resistances. The equivalent load resistance expression is shown as follows:

$$R_{Leq1} = \frac{8}{\pi^2} R_{L1}, \quad R_{Leq2} = \frac{8}{\pi^2} R_{L2}. \tag{3}$$

Every coil L_k is connected in series with a compensation capacitor C_k ($k = 1, 2, \ldots, 6$). L_{Rz1}, C_{Rz1}, and Z_{Rz1} compose the Rx compensation network of power channel #1. L_{Rz2}, C_{Rz2}, and Z_{Rz2} compose the Rx compensation network of power channel #2. Compensation network parameters can be obtained by (4) and (5). ω_0 represents the circuit resonance frequency of the coupler.

$$\omega_0 = \frac{1}{\sqrt{L_1 C_1}} = \frac{1}{\sqrt{L_2 C_2}} = \frac{1}{\sqrt{L_3 C_3}} = \cdots = \frac{1}{\sqrt{L_6 C_6}} \tag{4}$$

$$\omega_1 = \frac{1}{\sqrt{L_{Rz2} C_{Rz2}}}, \quad \omega_2 = \frac{1}{\sqrt{L_{Rz1} C_{Rz1}}}. \tag{5}$$

The compensation network with the band-stop filter can reduce the cross interference from the nontarget frequency to achieve the selective power distribution for two loads.

For power channel #1, the band-stop filter (L_{Rz1} and C_{Rz1}) is used to avoid the cross interference of power channel #2. However, the additional band-stop filter (L_{Rz1} and C_{Rz1}) itself will inevitably interfere with the power transfer in power channel #1. To solve the problem, we add Z_{Rz1} into the compensation network. Z_{Rz1} is a compensating element specifically for the band filter (L_{Rz1} and C_{Rz1}), and it can be a capacitor or an inductor.

Rx compensation network of power channel #1 (L_{Rz1}, C_{Rz1}, and Z_{Rz1}) needs to have a large impedance at ω_2 and zero impedance at ω_1 at the same time. This is also the case for the Rx compensation network of power channel #2 (L_{Rz2}, C_{Rz2}, and Z_{Rz2}). Therefore, Z_{Rz1} and Z_{Rz2} should be designed as follows:

$$\begin{cases} Z_{Rz1} = \frac{1}{\omega_1^2 C_{Rz1} - \frac{1}{L_{Rz1}}} \\ Z_{Rz2} = \frac{1}{\omega_2^2 C_{Rz2} - \frac{1}{L_{Rz2}}}. \end{cases} \tag{6}$$

In Fig. 4, Z_{Rc1} and Z_{Rc1} are marked with two dashed boxes in blue and red, respectively. Z_{Rc1} represents the impedance of power channel #1 Rx compensation network (L_{Rz1}, C_{Rz1}, and Z_{Rz1}). Z_{Rc2} represents the impedance of power channel #2 Rx compensation network (L_{Rz2}, C_{Rz2}, and Z_{Rz2}), which are expressed as follows:

$$\begin{cases} Z_{Rc1} = j\omega Z_{Rz1} + \frac{1}{j\omega C_{Rz1} + \frac{1}{j\omega L_{Rz1}}} \\ Z_{Rc2} = j\omega Z_{Rz2} + \frac{1}{j\omega C_{Rz2} + \frac{1}{j\omega L_{Rz2}}}. \end{cases} \tag{7}$$

When $\omega = \omega_1$, Z_{Rc1} and Z_{Rc2} can be transformed into the following:

$$\begin{cases} Z_{Rc1} = -\frac{1}{j\omega_1 C_{Rz1} + \frac{1}{j\omega_1 L_{Rz1}}} + \frac{1}{j\omega_1 C_{Rz1} + \frac{1}{j\omega_1 L_{Rz1}}} = 0 \\ Z_{Rc2} = j\omega_1 \frac{1}{\omega_1^2 C_{Rz2} - \frac{1}{L_{Rz2}}} + \frac{1}{j\omega_1 C_{Rz2} + \frac{1}{j\omega_1 L_{Rz2}}} = \infty. \end{cases} \tag{8}$$

When $\omega = \omega_2$, Z_{Rc1} and Z_{Rc2} can be transformed into the following:

$$\begin{cases} Z_{Rc1} = j\omega_2 \frac{1}{\omega_2 C_{Rz1} - \frac{1}{L_{Rz1}}} + \frac{1}{j\omega_2 C_{Rz1} + \frac{1}{j\omega_2 L_{Rz1}}} = \infty \\ Z_{Rc2} = -\frac{1}{j\omega_2 C_{Rz2} + \frac{1}{j\omega_1 L_{Rz2}}} + \frac{1}{j\omega_2 C_{Rz2} + \frac{1}{j\omega_2 L_{Rz2}}} = 0. \end{cases} \tag{9}$$

It can be found from (8) and (9) that Z_{Rc2} approaches infinity at ω_1 and 0 at ω_2, and the Z_{Rc1} approaches infinity at ω_2 and 0 at ω_1. Therefore, power channel #1 can be seen as an open circuit for voltage source $u_2(t)$, and Z_{Rc1} does not affect the power flow of power channel #1. Power channel #2 can be seen as an open circuit for voltage source u_1, and Z_{Rc2} does not affect the power flow of power channel #2. The impedance of Z_{Rc1} and Z_{Rc2} versus operating frequency is shown in Fig. 5. It can be found that two power channels are independent of each other.

The linear circuit satisfies the homogeneity and additivity. The equivalent circuit of the proposed system can be simplified, as shown in Fig. 6. $i_{kc1}(t)$ and $i_{kc2}(t)$ represent the induced current of L_k in power channel #1 and power channel #2. The equivalent circuits are the same for both channels, so only one of them needs to be modeled.

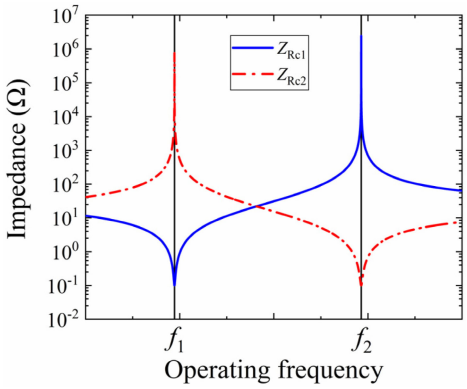

Fig. 5. Impedance of Z_{Rc1} and Z_{Rc2} versus operating frequency.

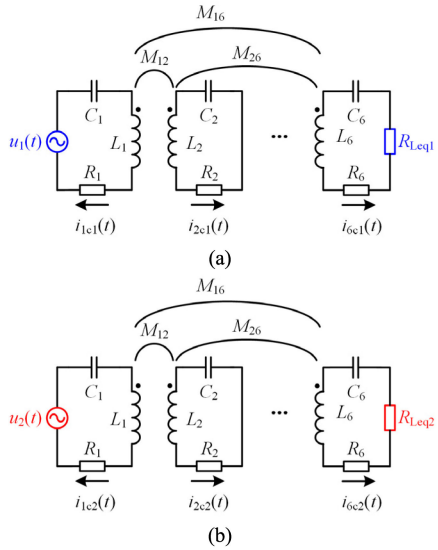

Fig. 6. Simplified equivalent circuit of a dual-frequency dual-load multirelay MC-WPT system based on shared power channel. (a) Power channel #1. (b) Power channel #2.

C. System Analysis

This article separately defines the matrix $\boldsymbol{L}$, the matrix $\boldsymbol{R}$, and the matrix $\boldsymbol{C}$ as (10)–(12)

$$\boldsymbol{L}=\begin{bmatrix} L_1 & M_{12} & \cdots & M_{16} \\ M_{12} & L_2 & \cdots & M_{26} \\ \vdots & \vdots & \ddots & \vdots \\ M_{16} & M_{26} & \cdots & L_6 \end{bmatrix} \tag{10}$$

$$\boldsymbol{R}_{c1}=\begin{bmatrix} R_1 & 0 & \cdots & 0 \\ 0 & R_2 & \cdots & 0 \\ \vdots & \vdots & \ddots & \vdots \\ 0 & 0 & \cdots & R_6+R_{Leq1} \end{bmatrix} \tag{11}$$

$$\boldsymbol{C}=\begin{bmatrix} C_1^{-1} & 0 & \cdots & 0 \\ 0 & C_2^{-1} & \cdots & 0 \\ \vdots & \vdots & \ddots & \vdots \\ 0 & 0 & \cdots & C_6^{-1} \end{bmatrix}. \tag{12}$$

According to Kirchhoff's voltages law, the underlying equation of the power channel #1 equivalent circuit expressed by the above three matrices is as follows:

$$\boldsymbol{L}\frac{d^2\boldsymbol{i}_{c1}(t)}{dt^2}+\boldsymbol{R}_{c1}\frac{d\boldsymbol{i}_{c1}(t)}{dt}+\boldsymbol{C}\boldsymbol{i}_{c1}(t)=\boldsymbol{H}\frac{du_1(t)}{dt} \tag{13}$$

where $\boldsymbol{i}_{c1}(t)=[i_{1c1}(t),\ i_{2c1}(t),\ \ldots\ ,i_{6c1}(t)]^T$ and $\boldsymbol{H}=[1\ 0\cdots\ 0]^T$.

Equation (14) is an $n\times n$ matrix polynomial of degree 2, and the coefficients of the matrix $\boldsymbol{Q}_{c1}(\lambda)$ are quadratic polynomials in the scalar λ. Matrix $\boldsymbol{Q}_{c1}(\lambda)$ is often called λ-matrix.

$$\boldsymbol{Q}_{c1}(\lambda)=\lambda^2\boldsymbol{L}+\lambda\boldsymbol{R}_{c1}+\boldsymbol{C}. \tag{14}$$

The spectrum of $\boldsymbol{Q}_{c1}(\lambda)$ is denoted by $\Lambda_{c1}(\boldsymbol{Q}_{c1})$, as shown in (15), and it is the set of the eigenvalues of $\boldsymbol{Q}_{c1}(\lambda)$. There are 12 eigenvalues in the proposed six-coil MC-WPT system

$$\begin{aligned}\Lambda_{c1}(\boldsymbol{Q}_{c1})&=\{\lambda\in\mathbb{C}:\det\boldsymbol{Q}_{c1}(\lambda)=0\}\\&=\operatorname{diag}(\lambda_{1c1},\lambda_{2c1},\ldots,\lambda_{11c1},\lambda_{12c1})\end{aligned} \tag{15}$$

where diag($\lambda_{1\,c1}, \lambda_{2\,c1}, \ldots, \lambda_{12\,c1}$) represents the diagonal matrix with $\lambda_{1\,c1}, \lambda_{2\,c1}, \ldots, \lambda_{12\,c1}$ as elements.

$\boldsymbol{L}$, $\boldsymbol{R}_{c1}$, and $\boldsymbol{C}$ are the real symmetric positive definite, so all eigenvalues are real or come in pairs (λ,λ^*). The real part of λ_k is the attenuation coefficient, and the imaginary part of λ_k is approximately equal to the system resonance frequency. A total of 12 eigenvalues can be divided into six pairs of eigenvalues, and only half of them ($\lambda_{1\,c1}, \lambda_{2\,c1}, \ldots, \lambda_{6\,c1}$) are needed to be analyzed for the output characteristics.

Let $\boldsymbol{X}_{c1}$ and $\boldsymbol{Y}_{c1}$ represent the eigenvectors of the $\boldsymbol{Q}_{c1}(\lambda)$. $\boldsymbol{x}_{kc1}$ and $\boldsymbol{y}_{kc1}$ are the right and left eigenvectors, respectively, corresponding to λ_{kc1}.

$$\begin{cases}\boldsymbol{X}_{c1}=[\boldsymbol{x}_{1c1},\boldsymbol{x}_{2c1},\ldots,\boldsymbol{x}_{11c1},\boldsymbol{x}_{12c1}]\\ \boldsymbol{Y}_{c1}=[\boldsymbol{y}_{1c1},\boldsymbol{y}_{2c1},\ldots,\boldsymbol{y}_{11c1},\boldsymbol{y}_{12c1}]\end{cases}. \tag{16}$$

When $\boldsymbol{L}$ is nonsingular and all the eigenvalues are simple, the solution of the homogeneous differential equation is shown in (17). For a stable MC-WPT system, the real parts of all eigenvalues are negative. The special solution decreases to zero as $t\to\infty$, so the steady-state-induced current is equal to the general solution

$$\begin{aligned}\boldsymbol{i}_{c1}(t)&=\boldsymbol{X}_{c1}e^{\Lambda_{c1}t}\left(\boldsymbol{\alpha}+\int_0^t e^{-\Lambda_{c1}s}\boldsymbol{Y}_{c1}\boldsymbol{H}u'_1(s)ds\right)\\&=\sum_{k=1}^{12}\frac{\boldsymbol{x}_{kc1}\boldsymbol{y}_{kc1}^*}{j\omega-\lambda_{kc1}}\boldsymbol{H}u'_1(t)\end{aligned} \tag{17}$$

where $\boldsymbol{\alpha}=[a_1,\ldots,a_{12}]^T$ and $\boldsymbol{H}=[1\ 0\cdots\ 0]^T$.

In the same way, $\boldsymbol{i}_{c2}(t)$ is expressed as (18). λ_{kc2} represents the eigenvalue of power channel #2. $\boldsymbol{x}_{kc2}$ and $\boldsymbol{y}_{kc2}$ are the right and left eigenvectors, respectively, corresponding to λ_{kc2}

$$\boldsymbol{i}_{c2}(t)=\sum_{k=1}^{12}\frac{\boldsymbol{x}_{kc2}\boldsymbol{y}_{kc2}^*}{j\omega-\lambda_{kc2}}\boldsymbol{H}u'_2(t) \tag{18}$$

where$\boldsymbol{i}_{c2}(t)=[i_{1c2}(t),\ i_{2c2}(t),\ \ldots\ ,i_{6c2}(t)]^T$.

The total current in each coil can be expressed as follows:

$$\boldsymbol{i}(t)=\boldsymbol{i}_{c1}(t)+\boldsymbol{i}_{c2}(t). \tag{19}$$

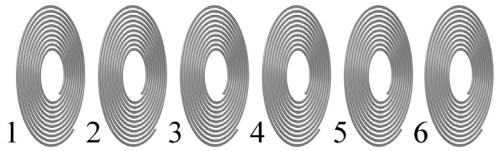

Fig. 7. Six-coil MC-WPT system. The normal lines of all coils are in the same direction, and the transmission distance *d* between the adjacent coils is the same.

TABLE I
SIMULATION SYSTEM PARAMETERS

Parameter	Value	Parameter	Value
number of turns	24	wire diameter	2 mm
layers of the coil	3	transmission distance d	50 mm
radii of the coil	100 mm	supply voltage V	100 V
inductance L_1,…, L_6	198.92 μH	ESR R_1,…, R_6	73.7 mΩ
capacitance C_1,…,C_6	930.16 pF	number of coils	6

TABLE II
MUTUAL INDUCTANCE VARYING WITH DIFFERENT TRANSMISSION DISTANCES

d (mm)	M (μH)
50	53.931
100	23.022
150	11.411
200	6.2601
250	3.7220

III. CONSTANT CURRENT OUTPUT CHARACTERISTICS

The methodology of constant current output characteristics is demonstrated with the use of a six-coil MC-WPT system, as shown in Fig. 7. The output characteristics of the two power channels are the same as each other because they share the same coupler. Hence, only one of the power channels needs to be analyzed.

The simulation system parameters are shown in Table I. The mutual inductance M varying with a different transmission distance d is shown in Table II.

A. Effect of Load Resistance on Eigenvalue

It can be seen from (17) that the output characteristics of the system are closely related to the eigenvalue, so the constant current frequencies can be obtained from eigenvalues [29].

According to (15), the variation of the eigenvalues with the equivalent load resistance R_{Leq} is shown in Fig. 8. λ_k represents λ_{kc1} or λ_{kc2}, and R_{Leq} represents R_{Leq1} or R_{Leq2}. As the R_{Leq} increases from 0 to 1000 Ω, six eigenvalues change in the direction shown by the arrow. The horizontal axis (Re) is the real part of the eigenvalue, and the vertical axis (Im) is the imaginary part of the eigenvalue.

The real part of λ_3 becomes much smaller than that of the other eigenvalues as R_{Leq} increases. The real part of λ_3 is negative. According to (17) and (18), the effect of an eigenvalue on the system output can be ignored when the attenuation coefficient of it is much smaller than that of the other eigenvalues. When R_{Leq} approaches infinity, the imaginary part of the eigenvalue

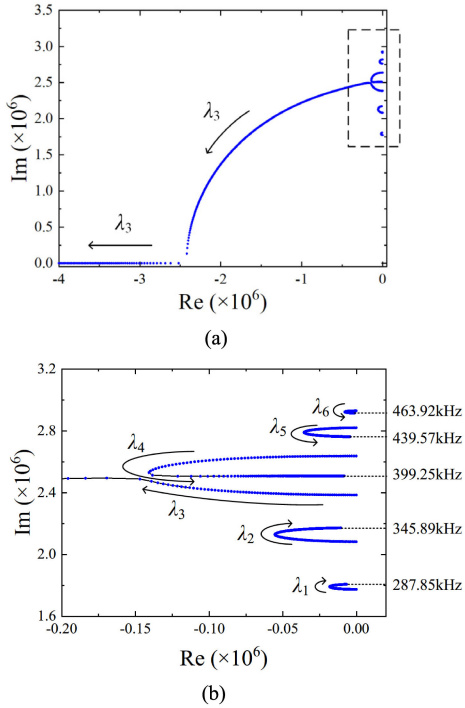

Fig. 8. Variation of the eigenvalues with the equivalent load resistance R_{Leq}. (a) Global eigenvalues. (b) Partial eigenvalues.

approaches a certain value. In particular, the imaginary part of λ_3 approaches 0 as R_{Leq} approaches infinity, and the system resonance frequency decreases from 6 to 5. When the load resistance is infinite (i.e., open circuit), the imaginary parts of the eigenvalues are defined as the strong damping frequencies (constant current frequencies) [29], as shown in the following:

$$\omega_{CC} = \{\omega \in \mathbb{R} : \mathrm{Im}(\lambda_k) \text{ with } R_{Leq} \to \infty\}. \tag{20}$$

B. Output Characteristics and Eigenvalues

In the multirelay WPT system, the system output currents are load independent at strong damping frequencies. The detailed calculation method of strong damping frequencies is as follows.

1) Let $\boldsymbol{R}_{CC}$ represent matrix $\boldsymbol{R}$ of the system. $\boldsymbol{R}_{CC}$ is expressed as (21). Then, we can get $\boldsymbol{Q}_{CC}(\lambda)$ by (22)

$$\boldsymbol{R}_{CC} = \mathrm{diag}\left(R_1\ R_2\ \ldots\ \infty\right) \tag{21}$$

$$\boldsymbol{Q}_{CC}(\lambda) = \lambda^2\boldsymbol{L} + \lambda\boldsymbol{R}_{CC} + \boldsymbol{C}. \tag{22}$$

2) Let $\boldsymbol{A}$ - $\lambda\boldsymbol{B}$ is a linearization of $\boldsymbol{Q}_{CC}(\lambda)$

$$\begin{cases} \boldsymbol{A} = \begin{bmatrix} \boldsymbol{C} & \boldsymbol{0} \\ \boldsymbol{0} & \boldsymbol{E} \end{bmatrix} \\ \boldsymbol{B} = \begin{bmatrix} -\boldsymbol{R}_{CC} & -\boldsymbol{L} \\ \boldsymbol{0} & \boldsymbol{E} \end{bmatrix} \end{cases} \tag{23}$$

where $\boldsymbol{E}$ is a sixth-order identity matrix.

3) By computing the generalized Schur decomposition, we obtain a numerically stable reduction, which is expressed

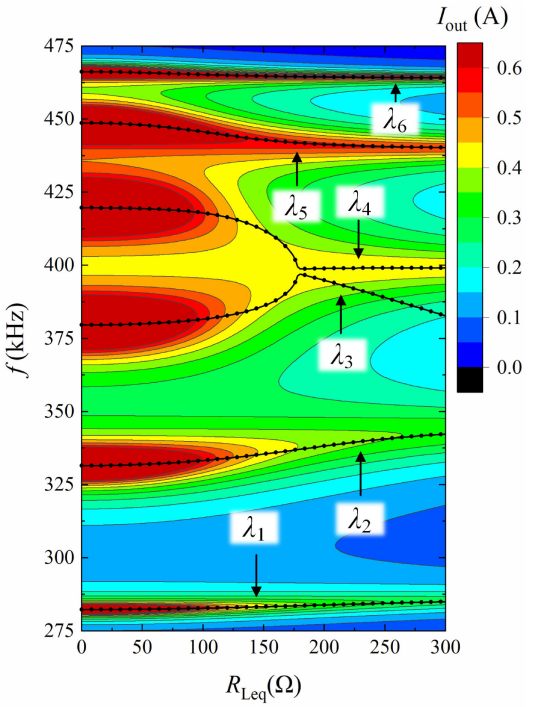

Fig. 9. I_{out} versus the operating frequency f and equivalent load resistance R_{Leq}.

as (24). $\Lambda(\boldsymbol{Q}_{\text{CC}})$ can be obtained from (25)

$$\begin{cases} \boldsymbol{W}^{*}\boldsymbol{A}\boldsymbol{Z} = \boldsymbol{S} \\ \boldsymbol{W}^{*}\mathbf{B}\mathbf{Z} = \mathbf{T} \end{cases} \tag{24}$$

where $\boldsymbol{S}$ and $\boldsymbol{T}$ are the upper triangles. $\boldsymbol{W}$ and $\boldsymbol{Z}$ are unitary.

$$\Lambda\left(\boldsymbol{Q}_{\text{CC}}\right) = \left\{ \frac{\boldsymbol{S}\left(i,i\right)}{\boldsymbol{T}\left(i,i\right)} \right\}. \tag{25}$$

4) The expression of constant current frequencies is shown as (26). ω_{CC} represents the constant current frequency

$$\omega_{\text{CC}} = \text{Im}\left(\Lambda\left(\boldsymbol{Q}_{\text{CC}}\right)\right). \tag{26}$$

According to (20) and (26), there are five constant current frequencies in the proposed system: 287.85, 345.89, 399.25, 439.57, and 463.92 kHz. According to (14) and (17), output current I_{out} versus the operating frequency f and equivalent load resistance R_{Leq} is shown in Fig. 9. The horizontal axis represents the equivalent load resistance R_{Leq}, the vertical axis represents the supply frequency f, and the black dot–dash line represents $\text{Im}(\lambda_k)/2\pi$ $(k = 1, 2, \ldots, 6)$. The color represents the output current I_{out} rms. I_{out} represents I_{out1} or I_{out2}. R_{Leq} represents R_{Leq1} or R_{Leq2}.

It can be seen from Fig. 9 that when the system operates at the strong damping frequencies, the output current remains almost unchanged with R_{Leq} changing. However, it can also be found that the output gains and sensitivities to the operating frequency of these constant current frequencies are different. For the proposed system, only two of them need to be selected as the operating frequencies, so it is necessary to give some indices to compare these output characteristics at different operating frequencies.

TABLE III
NORMALIZED OUTPUT CHARACTERISTIC INDICES

f (kHz)	G_{ave}	σ	ρ	τ
287.85	0	0.0104	0.1822	0.6025
345.89	0.2827	0	0.0634	0.7398
399.24	0.5894	0.0458	0	0.8479
439.57	0.8820	0.1920	0.1512	0.8463
463.92	1	1	1	0.3333

In addition, the more relay coils there are, the more constant current output frequencies can be selected. Generally, a n-coil MC-WPT system has $n-1$ constant current frequencies.

IV. OUTPUT CHARACTERISTIC INDEX

To choose the optimized operating frequency from all constant current frequencies, three output characteristic indices are proposed. The average gain G_{ave}, the load-independent index σ, and the average sensitive index of frequency ρ are defined as (27), (28), and (29). G_{ave} represents the average value of G in the entire R_{Leq} range. σ represents the degree to which G deviates from G_{ave} in the entire R_{Leq} range. ρ represents the degree to which G changes when f deviates from the constant current frequency. The load-independent characteristic is negatively correlated with σ, and the frequency sensitivity is also negatively correlated with ρ

$$G_{\text{ave}} = \frac{\int_{R_a}^{R_b} G\left(f, R_{Leq}\right) dR_{Leq}}{R_b - R_a} \tag{27}$$

$$\sigma = \frac{\int_{R_a}^{R_b} \left| \frac{G(f,R_{Leq}) - G_{\text{ave}}(f)}{G_{\text{ave}}(f)} \right| dR_{Leq}}{\left(R_b - R_a\right)} \tag{28}$$

$$\rho = \frac{\int_{R_a}^{R_b} \frac{dG(f,R_{Leq})}{df} dR_{Leq}}{R_b - R_a} \tag{29}$$

where $[R_a, R_b]$ represents the range of R_{Leq}, and the G represents the function of system output current gain with operating frequency f and equivalent load resistance R_{Leq}, which are expressed as follows:

$$G\left(f, R_{Leq}\right) = 2\frac{I_{\text{out}}}{V}. \tag{30}$$

To comprehensively compare the three indices, this article gives the same weight to three indices and combines them into a comprehensive index τ, as shown in the following:

$$\tau = \frac{1}{3}\text{norm}\left(G_{\text{ave}}\right) + \frac{1}{3}\left(1 - \text{norm}\left(\sigma\right)\right) + \frac{1}{3}\left(1 - \text{norm}\left(\rho\right)\right) \tag{31}$$

where norm(…) represents the normalization.

The normalized output characteristic indices for five constant current frequencies are shown in Table III. The normalized method is Min–Max scaling. The linear function transforms the original data into the range [0 1]. The equivalent load resistance R_{Leq} ranges from 70 to 100 Ω.

There are significant differences in the output characteristic indices of five constant current frequencies (287.85, 345.89, 399.25, 439.57, and 463.92 kHz) among the average gain G_{ave},

the load-independent index σ, and the average sensitive index of frequency ρ.

It can be found from Table III that the output characteristic indices of 463.92 kHz are all higher than that of the other frequencies. However, the high σ and the high ρ are usually not beneficial to the proposed system. The high load-independent index σ means that I_{out} is very sensitive to R_{Leq}. The high average sensitive index of frequencies ρ means the high-precision operating frequency. Therefore, τ of 463.92 kHz is the lowest, and it is not suitable to be selected as the operating frequency G_{ave} of 287.85 kHz is lower than that of 345.89, 399.25, and 439.57 kHz, and ρ of 287.85 kHz is higher than that of 345.89, 399.25, and 439.57 kHz, so it is also not suitable to be selected as the operating frequency.

By comparison, the output characteristic indices of 345.89, 399.25, and 439.57 kHz are better, which are constant current frequencies with the top three comprehensive indices τ. The average gain G_{ave} is relatively high. The load-independent index σ and the average sensitive index of frequency ρ are relatively low. It should be noted that the operating frequencies of the two power channels should not be too close to each other because of the cross interference. Therefore, 345.89 and 439.57 kHz are finally selected as optimized operating frequencies.

In this article, a six-coil MC-WPT system is analyzed as an example. For the variation of the coil number, the system design method is still applicable. The design process is the same, and the details are as follows.

1) We first define $\boldsymbol{L}$, $\boldsymbol{R}$, and $\boldsymbol{C}$ according to (10), (11), and (12).
2) Constant current frequencies can also be obtained by (21)–(26). We choose the appropriate operating frequencies according to the comprehensive index τ, as shown in (31).
3) The compensation network parameters of power channel #1 and power channel #2 can be obtained by (5) and (6).

V. Simulation and Experimental Verification

A. Experimental Setup and Simulation Model

A simulation model of the MC-WPT system is built according to Fig. 2. An experimental setup of the multirelay MC-WPT system is built, as shown in Fig. 10, to verify the dual-frequency dual-load multirelay MC-WPT system proposed in this article. The setup consists of a dc power supply (ITECH IT6535D), an inverter, a coupler, a dc electronic load (ITECH IT8512A+), a laptop, and a digital storage oscilloscope (Tektronix TPS 2024B).

The inverter employs SiC MOSFET (IMZ120R045M1) and is programmed by TI Code Composer Studio and implemented by the DSP controller (TMS320F28335).

The geometric parameters of the experimental setup are the same as the parameters in Table I. The coupler parameters are listed in Table IV, which are measured by HIOKI LCR meter IM3536.

The parameters of the Rx compensation network are calculated by (5) and (6). The Rx compensation parameters of the experimental setup are shown in Table V. In power channel #1, Z_{Rz1} is a capacitor that is equal to 21.15 nF. In power channel #2, Z_{Rz2} is an inductor that is equal to 6.171 μH.

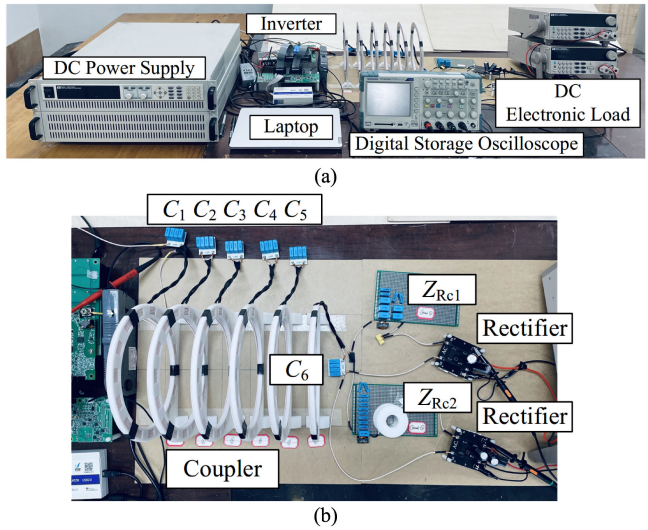

Fig. 10. Photograph of the experimental setup. (a) Overall. (b) Partial.

TABLE IV
Coupler Parameters of the Experimental Setup

Parameter	Value
L_1 … L_6 (μH)	219.4, 220.5, 219.3, 220.4, 220.8, 218.7
C_1 … C_6 (pF)	840, 841, 843, 832, 835, 842
R_1 … R_6(Ω)	1.68, 1.68, 1.68, 1.67, 1.77, 1.68
M_{12} … M_{16} (μH)	63.9, 28.8, 15.4, 8.58, 7.60
M_{23} … M_{26} (μH)	65.6, 30.0, 15.9, 8.88
M_{34} … M_{36} (μH)	67.5, 30.2, 15.6
M_{45} … M_{46}(μH)	68.3, 30.1
M_{56} (μH)	64.5

TABLE V
Compensation Network Parameters of the Experimental Setup

Parameter	Value	Parameter	Value
f_1	347.22 kHz	f_2	446.43 kHz
L_{Rz1}	3.922 μH	L_{Rz2}	4.031 μH
C_{Rz1}	32.42 nF	C_{Rz2}	52.13 nF
Z_{Rz1}	21.15 nF	Z_{Rz2}	6.171 μH

B. Simulation Results

The dual-frequency inverter output voltage and current of the simulation model are shown in Fig. 11. In the dual-frequency inverter, two operating frequencies are generated and controlled. The waveform of the current is the superposition of the two operating frequencies. Fig. 12 shows the voltages and currents on the receiver side before the rectifier. It can be seen from Fig. 12 that, as the load resistance increases, the current waveform will be distorted. However, it will not affect the output characteristics of the system, and the two power channels still have constant current output characteristics.

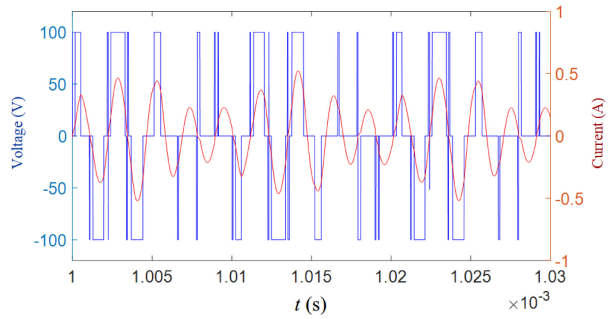

Fig. 11. Output voltage of the full-bridge inverter when R_{L1} and $R_{L2} = 70\ \Omega$.

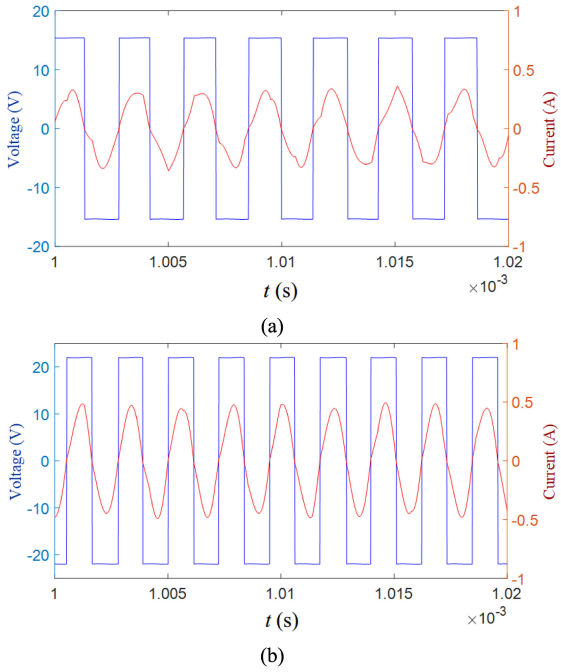

Fig. 12. Voltages and currents on the receiver side before the rectifier when R_{L1} and $R_{L2} = 70\ \Omega$. (a) Power channel #1. (b) Power channel #2.

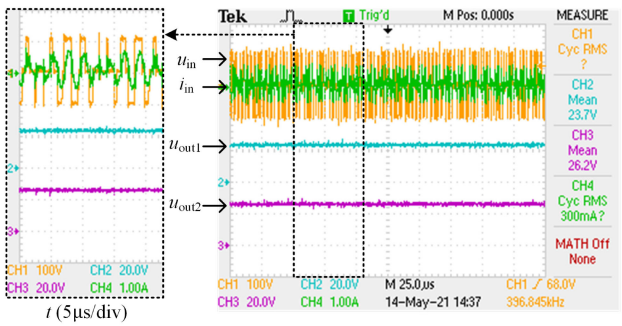

Fig. 13. Measured waveforms of voltage and current in the Tx and the Rx when R_{L1} and $R_{L2} = 100\ \Omega$.

C. Experimental Results

Fig. 13 illustrates the measured waveforms of input voltage $u_{\rm in}$, input current $i_{\rm in}$, and output voltages $u_{\rm out1}$ and $u_{\rm out2}$. The square wave voltage of two operating frequencies (347.22 kHz and 446.43 kHz) is generated by the inverter. Inducted currents

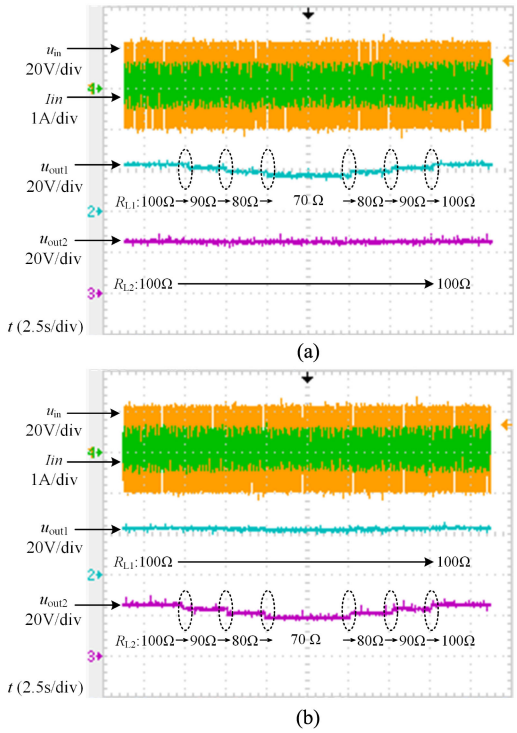

Fig. 14. Measured output waveforms with different load resistances. (a) $R_{L2} = 100\ \Omega$. (b) $R_{L1} = 100\ \Omega$.

of two frequencies are transmitted to the load resistance of the corresponding power channel by the shared power channel (shared coupler). Output voltage $U_{\rm out1}$ of power channel #1 is 23.7 V, and output voltage $U_{\rm out2}$ of power channel #2 is 26.2 V. The measured overall (dc–dc) power transfer efficiency of the experimental setup is 68.6%.

Fig. 14 shows the dynamic process of $u_{\rm in}$, $i_{\rm in}$, $u_{\rm out1}$, and $u_{\rm out2}$ with the variation of the load resistance. The range of load resistance is from 70 to 100 Ω. It can be seen from Fig. 14 that the changing load resistances in two power channels does not affect each other.

Fig. 15 shows the output currents, efficiencies, and output power with the different load resistances. For power channel #1, the resistance load R_{L1} is changed from 70 to 100 Ω. It can be seen from Fig. 15(a) that $I_{\rm out1}$ can be maintained to a relatively stable state and $I_{\rm out2}$ remains almost the same. The $I_{\rm out1}$ decreases from 0.256 to 0.236 A. The measured overall (dc–dc) power transfer efficiency increases from 67.1% to 68.6%. The range of theoretical power transfer efficiency is from 76.1% to 76.7%.

For power channel #2, the resistance load R_{L2} is changed from 70 to 100 Ω. It can be seen from Fig. 15(b) that $I_{\rm out2}$ can be maintained to a relatively stable state and $I_{\rm out1}$ remains almost the same. The $I_{\rm out1}$ decreases from 0.287 to 0.263 A. The measured overall (dc–dc) power transfer efficiency increases from 67.5% to 68.6%. The range of theoretical power transfer efficiency is from 76.4% to 76.8%.

The experimental results verify the constant current output characteristics of the two power channels. The transfer power range of the experimental setup is from 11 to 12.5 W, which

TABLE VI
COMPARISON OF THE SURVEYED SYSTEMS AND THE PROPOSED SYSTEM

Ref	Frequencies of WPT	Load	Relay coil	Compensation	Output characteristic	Selective power distribution	Efficiency
[13]	393 kHz	single	yes	SS	no	-	60%
[15]	547.7 kHz	single	no	LCC-S	constant voltage	-	32.5%
[16]	100 to 600 kHz	single	no	SS	no	-	68.2%
[19]	6.78 MHz	single	no	SS	no	-	57%
[21]	100 kHz, 300 kHz	multiple	no	SS	no	yes	90.7%
[22]	200 kHz	multiple	yes	LCC-S	constant voltage	no	63.7%
[23]	300 kHz	multiple	yes	SS	constant current	no	60%
[24]	98–300 kHz, 6.78 MHz	multiple	no	SS	no	yes	65%
proposed	347.22 kHz, 446.43 kHz	multiple	yes	SS	constant current	yes	68.6%

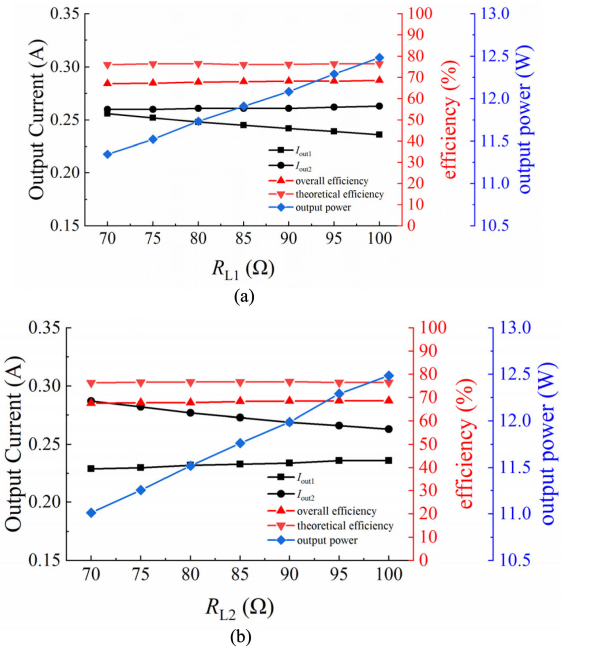

Fig. 15. Output currents, efficiencies, and output power with different load resistances. (a) $R_{L2} = 100\ \Omega$. (b) $R_{L1} = 100\ \Omega$.

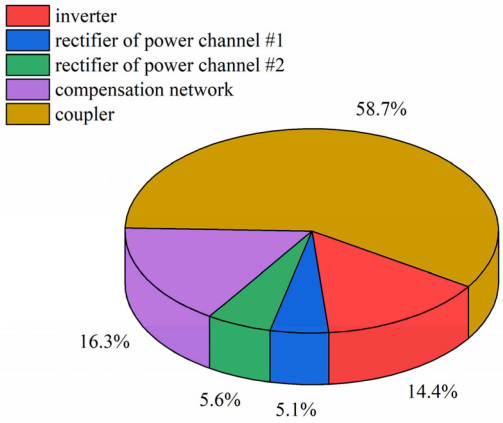

Fig. 16. Loss distribution of the proposed WPT system when $R_{L2} = 100\ \Omega$ and $R_{L1} = 100\ \Omega$.

can meet the power requirement of most online monitoring equipment.

Fig. 16 shows the loss distribution of the proposed system when R_{L1} and R_{L2} are 100 Ω [30]. The total loss is 5.71 W. Because there are six coils in the experimental setup, the coupler loss is the highest at 58.7%.

D. Discussion

To illustrate the advantages of the proposed system, a comprehensive comparison of the surveyed systems and the proposed system is given in Table VI. It can be observed that the proposed system takes the advantage of multiple constant current frequencies of the multirelay MC-WPT system, which are suitable to supply power for online monitoring equipment of the HVTL. However, the proposed system still has much room to improve in terms of efficiency. In future research, we can improve efficiency by optimizing the number of coil turns, compensating network parameters, and the system resonant frequency.

It should be noted that the proposed system design method is also helpful for the multirelay WPT system with three or more outputs. The constant current frequencies can also be obtained by (26). However, the topology needs improvement. The multifrequency inverter and the Rx compensation network need further research.

Moreover, compared with the common method to power multiple loads (e.g., the voltage regulator and the switching mode power supply), the downside of the proposed system is the inability to switch the output characteristics (constant voltage or constant current). In future research, we may achieve it by switching the compensation network or other methods to expand the application and scenario.

Finally, the effect of gap variation on system output characteristics is also a valuable research direction. Frequency control is a promising solution to this problem. If the coil gaps have changed greatly, adjusting the operating frequency of the inverter may make the system work normally again.

VI. CONCLUSION

A dual-frequency dual-load multirelay MC-WPT system based on the shared power channel is proposed, which provides

the constant current output characteristic and realizes the selective power distribution. Two operating frequencies are introduced by a full-bridge inverter. The proposed system is modeled by QEP, and all constant current frequencies are obtained. Three output characteristic index defines the performance of the system at different operating frequencies, which include the average gain, the load-independent index, and the average sensitive index of frequency. The experimental setup is built. The experimental results show that the theoretical results of the constant current frequency are consistent with the experimental results. Therefore, the feasibility and effectiveness of the dual-frequency multirelay MC-WPT system were verified. The proposed dual-frequency dual-load MC-WPT system is helpful for the application of the MC-WPT system.

REFERENCES

[1] J. Han, J. Hu, Y. Yang, Z. Wang, S. X. Wang, and J. He, "A nonintrusive power supply design for self-powered sensor networks in the smart grid by scavenging energy from ac power line," *IEEE Trans. Ind. Electron.,* vol. 62, no. 7, pp. 4398–4407, Jul. 2015.

[2] W. Wang, C. Xu, C. Zhang, and C. Chen, "Start-up and saturation optimization of high-power energy harvester with compound topologies overhead ac transmission line," *IEEE J. Emerg. Sel. Topics Power Electron.,* vol. 8, no. 4, pp. 3609–3617, Dec. 2020.

[3] Z. Wang et al., "A self-sustained current sensor for smart grid application," *IEEE Trans. Ind. Electron.*, vol. 68, no. 12, pp. 12810–12820, Dec. 2021.

[4] X. Dai, J. Wu, J. Jiang, R. Gao, and U. K. Madawala, "An energy injection method to improve power transfer capability of bidirectional WPT system with multiple pickups," *IEEE Trans. Power Electron.,* vol. 36, no. 5, pp. 5095–5107, May 2021.

[5] Y. Fan, Y. Sun, X. Dai, Z. Zuo, and A. You, "Simultaneous wireless power transfer and full-duplex communication with a single coupling interface," *IEEE Trans. Power Electron.,* vol. 36, no. 6, pp. 6313–6322, Jun. 2021.

[6] X.-D. Qing, Z.-H. Wang, Y.-G. Su, Y.-M. Zhao, and X.-Y. Wu, "Parameter design method with constant output voltage characteristic for bilateral LC-compensated CPT system," *IEEE J. Emerg. Sel. Topics Power Electron.,* vol. 8, no. 3, pp. 2707–2715, Sep. 2020.

[7] W. Zhou, Y.-G. Su, L. Huang, X.-D. Qing, and A. P. Hu, "Wireless power transfer across a metal barrier by combined capacitive and inductive coupling," *IEEE Trans. Ind. Electron.,* vol. 66, no. 5, pp. 4031–4041, May 2019.

[8] C. Xia, N. Wei, H. Zhang, S. Zhao, Z. Li, and Z. Liao, "Multifrequency and multiload MCR-WPT system using hybrid modulation waves SPWM control method," *IEEE Trans. Power Electron.*, vol. 36, no. 11, pp. 12400–12412, Nov. 2021.

[9] N. U. Hassan, S.-W. Hong, and B. Lee, "A robust multioutput self-regulated rectifier for wirelessly powered biomedical applications," *IEEE Trans. Ind. Electron.,* vol. 68, no. 6, pp. 5466–5472, Jun. 2021.

[10] S.-H. Lee et al., "Voltage-boosted current-mode wireless power receiver for directly charging a low-voltage battery in implantable medical systems," *IEEE Trans. Ind. Electron.,* vol. 66, no. 11, pp. 8860–8865, Nov. 2019.

[11] X. Dai, J.-C. Jiang, and J.-Q. Wu, "Charging area determining and power enhancement method for multiexcitation unit configuration of wirelessly dynamic charging EV system," *IEEE Trans. Ind. Electron.,* vol. 66, no. 5, pp. 4086–4096, May 2019.

[12] M. Xiong, X. Wei, Y. Huang, Z. Luo, and H. Dai, "Research on novel flexible high-saturation nanocrystalline cores for wireless charging systems of electric vehicles," *IEEE Trans. Ind. Electron.*, vol. 68, no. 9, pp. 8310–8320, Sep. 2021.

[13] C. Zhang, D. Lin, N. Tang, and S. Y. R. Hui, "A novel electric insulation string structure with high-voltage insulation and wireless power transfer capabilities," *IEEE Trans. Power Electron.*, vol. 33, no. 1, pp. 87–96, Jan. 2018.

[14] W. Wang, X. Huang, L. Tan, J. Zhao, and C. Yan, "Hybrid wireless charging system for monitoring overhead 110 kV high-voltage power line equipment based on magneto-electric conversion," *IET Gener., Transmiss. Distrib.,* vol. 10, no. 5, pp. 1199–1208, Apr. 2016.

[15] C. Cai et al., "Resonant wireless charging system design for 110-kV high-voltage transmission line monitoring equipment," *IEEE Trans. Ind. Electron.*, vol. 66, no. 5, pp. 4118–4129, May 2019.

[16] H. Zhou, X. Gao, J. Lai, W. Hu, Q. Deng, and D. Zhou, "Natural frequency optimization of wireless power systems on power transmission lines," *IEEE Access,* vol. 6, pp. 14038–14047, 2018.

[17] M. Xingkui, H. Qisheng, X. Yudi, L. Shifa, Z. Zhe, and M. A. E. Andersen, "Wireless power supply via coupled magnetic resonance for on-line monitoring wireless sensor of high-voltage electrical equipment," in *Proc. 42nd Annu. Conf. IEEE Ind. Electron. Soc.*, Washington, DC, USA, 2016, pp. 4582–4587.

[18] J. Chen, Z. Hu, S. Wang, Y. Cheng, and M. Liu, "Investigation of wireless power transfer for smart grid on-line monitoring devices under HV condition," *Procedia Comput. Sci.*, vol. 83, pp. 1307–1312, 2016.

[19] S.-H. Lee, K.-P. Yi, and M.-Y. Kim, "6.78-MHz, 50-W wireless power supply over a 60-cm distance using a GaN-based full-bridge inverter," *Energies,* vol. 12, no. 3, Feb. 2019, Art. no. 371.

[20] J. Qu, L. He, N. Tang, and C.-K. Lee, "Wireless power transfer using domino-resonator for 110-kV power grid online monitoring equipment," *IEEE Trans. Power Electron.,* vol. 35, no. 11, pp. 11380–11390, Nov. 2020.

[21] Z. Zhang, X. Li, H. Pang, H. Komurcugil, Z. Liang, and R. Kennel, "Multiple-frequency resonating compensation for multichannel transmission of wireless power transfer," *IEEE Trans. Power Electron.,* vol. 36, no. 5, pp. 5169–5180, May 2021.

[22] C. Cheng, W. Li, Z. Zhou, Z. Deng, and C. Mi, "A load-independent wireless power transfer system with multiple constant voltage outputs," *IEEE Trans. Power Electron.,* vol. 35, no. 4, pp. 3328–3331, Apr. 2020.

[23] C. Cheng et al., "A multiload inductive power transfer repeater system with constant load current characteristics," *IEEE J. Emerg. Sel. Topics Power Electron.*, vol. 8, no. 4, pp. 3533–3541, Dec. 2020.

[24] C. K. Lee, W. X. Zhong, and S. Y. R. Hui, "Effects of magnetic coupling of nonadjacent resonators on wireless power domino-resonator systems," *IEEE Trans. Power Electron.,* vol. 27, no. 4, pp. 1905–1916, Apr. 2012.

[25] C. Zhao and D. Costinett, "GaN-based dual-mode wireless power transfer using multifrequency programmed pulse width modulation," *IEEE Trans. Ind. Electron.,* vol. 64, no. 11, pp. 9165–9176, Nov. 2017.

[26] F. Liu, Y. Yang, Z. Ding, X. Chen, and R. M. Kennel, "A multifrequency superposition methodology to achieve high efficiency and targeted power distribution for a multiload MCR WPT system," *IEEE Trans. Power Electron.,* vol. 33, no. 10, pp. 9005–9016, Oct. 2018.

[27] Z. Pantic, K. Lee, and S. M. Lukic, "Receivers for multifrequency wireless power transfer: Design for minimum interference," *IEEE J. Emerg. Sel. Topics Power Electron.,* vol. 3, no. 1, pp. 234–241, Mar. 2015.

[28] W. Zhong and S. Y. R. Hui, "Auxiliary circuits for power flow control in multifrequency wireless power transfer systems with multiple receivers," *IEEE Trans. Power Electron.,* vol. 30, no. 10, pp. 5902–5910, Oct. 2015.

[29] X. Hou, Y. Su, Z. Zuo, X. Dai, and Y. Fei, "A novel analysis method based on quadratic eigenvalue problem for multirelay magnetic coupling wireless power transfer," *IEEE Trans. Power Electron.,* vol. 36, no. 9, pp. 9907–9917, Sep. 2021.

[30] B. X. Nguyen et al., "An efficiency optimization scheme for bidirectional inductive power transfer systems," *IEEE Trans. Power Electron.,* vol. 30, no. 11, pp. 6310–6319, Nov. 2015.

Xinyu Hou received the B.E. degree in 2017 from the College of Automation, Chongqing University, Chongqing, China, where he is currently working toward the Ph.D. degree in control theory and control engineering.

His research interests include multirelay wireless power transfer and foreign object detection technology.

Zhihui Wang (Member, IEEE) received the B.S. and M.S. degrees in automation and the Ph.D. degree in control theory and control engineering from the College of Automation, Chongqing University, Chongqing, China, in 2003, 2006, and 2009, respectively.

He is currently a Professor with the College of Automation, Chongqing University. His current research interests include both fundamental investigations and practical engineering applications in efficient high-power converters and wireless power supply.

Yugang Su (Member, IEEE) received the B.E. and M.E. degrees in industry automation and the Ph.D. degree in control theory and control engineering from Chongqing University, Chongqing, China, in 1985, 1993, and 2004, respectively.

From 2008 to 2009, he was a Visiting Scholar with the University of Queensland, Brisbane, QLD, Australia. He is currently a Professor with the College of Automation, Chongqing University. His research interests include power electronics, control theory and applications, and wireless power transfer.

Zhe Liu received the B.E. degree in electrical engineering from the Chongqing University of Technology, Chongqing, China, in 2014, and the M.E. degree from the College of Electrical Engineering, Kunming University of Science and Technology, Kunming, China, in 2017. He is currently working toward the Ph.D. degree in control theory and control engineering with the College of Automation, Chongqing University, Chongqing, China.

His research interests include capacitive power transfer and the single capacitive coupled wireless power transfer.

Zhipeng Deng received the B.E. degree from the Hubei University of Automotive Technology, Shiyan, China, in 2017, and the M.E. degree in 2020 from Chongqing University, Chongqing, China, where he is currently working toward the Ph.D. degree in control theory and control engineering with the College of Automation.

His current research interests include modeling and control of wireless power transfer and power electronics. He is also working on wireless power transfer for the application of electric vehicle charging.